Three-dimensional modelling and simulation of the vibration mark on surface generation in ultra-precision grinding

Chen Shanshan[1,2], Cheung Chi Fai [1*], Zhang Feihu[2], Zhao, Chenyang[1]

1 Partner State Key Laboratory of Ultraprecision Machining Technology, Department of Industrial and Systems Engineering, The Hong Kong Polytechnic University, Hung Hom, Kowloon, Hong Kong

2 Harbin Institute of Technology, School of mechanical and electrical engineering, Harbin, China

*Corresponding author: benny.cheung@polyu.edu.hk Fax: (852)23625267

Abstract: Nowadays, most modelling work for ground surface topography is based on either abrasive kinematics (micro-level) or high-frequency vibration of the grinding wheel (macro-level) to predict surface quality or grinding performance, but there is a lack of a correlation model to relate these two levels together. In this research work, wheel shape with two radii and wheel synchronous vibration are modelled first for the interference of the tool edge in 3D space to reveal the evolution mechanism of surface waviness under different phase shifts (0.0-1.0). Hence, a multi-scale model is established considering the diverse protrusion heights of the grits and incorporating the wheel shape and micro-vibration of the tool so as to explain the mechanism of the generation of the surface marks on the ground surface. The result shows that four principal residual marks are formed on the ground surface including spirals, tool feed marks, cumulative phase marks and abrasive grain scratches. The amount of surface waviness resulting from the tool unbalance is equal to the ratio of the rotating speed of the grinding wheel and the workpiece. The feed mark representing the tool locus and tool nose geometry is a spiral pattern from edge area to the machined centre. The vibration marks are caused by the phase accumulation effect. The grit scratches are related to the wheel geometry, kinematics and distribution of protrusion heights. In addition, the phase shift tends to increase the density of grinding marks, with a significant decrease when the phase shift is equal to 0.5. The surface generation model is further verified by a closed surface matching method, which shows the simulation results agree reasonably well with the grinding experiments.

Key words: Wheel geometry, Grinding, Surface generation, Phase shift, Micro-vibration; Ultra-precision machining

1 Introduction

Ultra-precision grinding is widely applied to precision manufacture a wide range of materials and components with different geometries, which can achieve remarkable workpiece tolerance and accuracy. With the technological advancement of ultra-precision grinding machine with high stiffness and high accuracy, it is feasible to machine hard and brittle materials, such as silicon carbide (SiC), silicon nitride (Si_3N_4) and tungsten carbide (WC) without inducing fracture damage [1-3]. Ceramic materials are typically difficult-to-machine materials due to their extremely high hardness and fragility [4-7]. Due to the outstanding properties of chemical inertness and wear resistance of silicon carbide (SiC) for engineering ceramics as

compared to traditional metallic materials [8,9], it has been applied not only to machine structural components but also precision optical parts in recent years [10-12]. Ultra-precision diamond grinding is more properly used to machine SiC due to its high material removal rate and is able to achieve favourable surface integrity [13]. Form accuracy and surface quality have become the key indicators to evaluate the preference of the grinding process. To achieve a mirror-finished surface without fracture damage, considerable research work has been devoted to studying the cutting mechanics and surface generation mechanisms in ultra-precision grinding.

However, ultra-precision grinding is a complex process, which is influenced by many factors, such as the workpiece material, wheel characteristics and grinding conditions. The modelling of the surface generation is more complicated than that of single point turning (SPDT) or multipoint milling [14]. In recent years, with the increasing demand for a high degree of accuracy and high-resolution optical systems, there is growing demand for high surface quality and integrity of machined workpieces. Improving the surface quality of optical components is a critical issue in ultra-precision grinding. To better understand the process of surface generation in ultra-precision grinding, a theoretical surface generation model is of great need to be developed to explain the interaction of grinding wheel and workpiece. There are two ways to establish a surface generation model, i.e. empirical approach and analytical approach. For the empirical approach, surface roughness prediction is performed based on a large number of machining experiments in order to calculate the coefficients in polynomials. The analytical approach is based on studying the geometrical relationships between the cutting edges and the workpiece so as to determine the surface topography. In comparison to empirical models, an analytical approach is preferable due to its better predictability and suitability under a wide range of cutting conditions [15]. A large number of analytical models have been developed, which are focused on studying the surface generation mechanisms so as to trace and track the optimal cutting parameters [16-19]. Tool characterization is a key aspect to model surface finish, mostly adopting statistical analysis to define a random distribution function of grits with different protrusion heights, and kinetical analysis is used to describe the cutting event so as to determine the surface roughness [20-23]. CHENG, et al. [24], proposed a geometrical model of surface roughness in the micro-grinding of soda-lime glass by considering different densities and protrusion heights of abrasive grains. In the model, the different densities for various protrusion heights are deterimined and the low surface roughness can be achieved with a fine feed rate and high speed for the grinding wheel. Liu, et al. [25] estabilished a theoretical model to predict the workpiece surface roughness by considering the different shapes of grains. In this research, sphere, truncated cone and cone abrasive grains combining the dressing condition are considered to predict the surface roughness and it was found that the dressing is the dominant factor deterimining the final surface roughness. McDonald, et al. [26] developed a kinematic model for surface generation and the undeformed chip thickness based on experimentally measuring the grinding wheel topography. In order to enhance the computational efficiency, a new peak-removal method is proposed to remove erroneous spikes. Aleksandrova [27], presented a model to optimize the dressing parameters in cylindrical grinding by a

generalized unility function, which related the tool life, machininability, and grinding force to the dressing parameters.Kuriyagawa , et al. [28], study the nano-topography generation in grinding of axisymmetric aspherical surface and analyze the relationship between workpiece and wheel revolution speeds and machining marks caused by the nano-topography. Yoshihara, et al. [28], developed a new model to describe the cross sectional profile of the ground surface resulted from the unbalenced vibration of grinding wheel in machining axisymetric surface. In this model, the arc-shaped wheel is considered and spatial frequency analyse is conducted to uncover the changes of the amplitude of the cross sectional profile of the machined surface in the direction of grinding wheel feed. In considering both the wheel topography and relative vibration, CAO, et al. [29], adopted the gaussian distribution function combined with the umblance vibration of the grinding wheel to drive the trajectory of each abrasive grain and simulate surface topography generation in cutting direction, in which the influence of grinding operation parameters, grit size and vibration amplitude of the wheel on the surface roughness and waviness was studied.

However, this modelling work for ground surface generation is mainly based on either the abrasive kinematics (micro-level) or high-frequency vibration of the wheel (macro-level) to predict surface generation or evaluate the performance of the grinding process. There is a lack of a compressive model to study surface generation in detail. In grinding operation, imbalance of the grinding wheel is not uncommon and results in changes of abrasive grain trajectories, in turn impacting on the machined surface, especially the phase shift which has a remarkable influence on the evolution of surface generation. In this paper, a theoretical model is established to study the influence of phase shift on surface waviness and grain trace on the surface quality of the ground workpiece so as to reveal the fundamental mechanism of grinding mark generation on ground surfaces.

2. Modelling of Phase Shift in Ultra-precision Grinding

In this study, contour grinding operation for flat surface was considered. Grinding is a complex machining process with a large number of parameters which affect the surface generation in the grinding process. It is almost impossible to conduct kinematics analysis by considering all the factors. As a result, it is necessary to make some simplifications in the modelling. Some assumptions were made as follows:

(i) Wheel wear effect and the movement errors of the workpiece spindle were ignored;

(ii) The vibration amplitude of the grinding wheel was kept stable at all rotational speeds (39000 RPM-40500 RPM);

(iii) The deformations of the wheel and workpiece were not considered; only the geometrical removal of material was considered without ploughing and rubbing phenomena.

2.1 Modelling of grinding wheel geometry

In ultra-precision grinding, a rotary part feeds over a spinning wheel with a constant feed rate to remove the materials

from the workpiece, as shown in Figure 1. The grinding wheel has a small tool nose radius (r) on the wheel edge and a large wheel radius (R), which can be approximated to a three-dimensional ellipsoid, as shown in Figure 1. In general, the tool nose radius is significantly larger than the depth of cut, the former measured at millimetre scale with the latter characterized in the micrometre range. As a result, the tool nose profile at the cutting edge determines the surface topography of the ground workpiece. The radius of curvature of the ellipse arc and the contact area of the tool nose radius at the lowest contact point can be considered to be equivalent due to the super small contact region between the wheel and the workpiece.

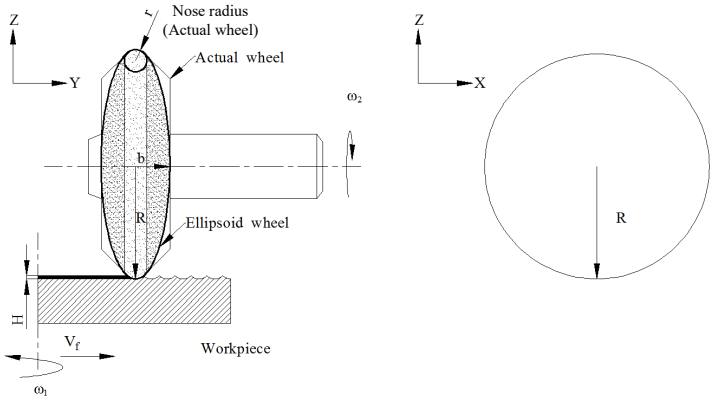

(a) (b)

Fig. 1. Illustration of the ellipsoid model for the grinding wheel: wheel geometry (a) in the Z-Y plane, (b) in the Z-X plane

The ellipsoid is expressed by Eq. (1) and its centre is set at the origin.

$$\frac{x^2}{R^2}+\frac{y^2}{b^2}+\frac{z^2}{R^2}=1 \tag{1}$$

However, the minor axis of the ellipsoid (b) is unknown, so to calculate b, the instantaneous curvature radius (r') in z-y section is derived as below:

$$r'=\frac{1}{\rho}=\frac{\left[1+\left(\frac{\partial z}{\partial y}\right)^2\right]^{\frac{3}{2}}}{\left|\frac{\partial^2 z}{\partial y^2}\right|} \tag{2}$$

In the z-y coordinate system, an ellipse is shown in Eq. (3):

$$\frac{y^2}{b^2}+\frac{z^2}{R^2}=1 \tag{3}$$

where:

$$z=\pm\sqrt{R^2\left(1-\frac{y^2}{b^2}\right)} \tag{4}$$

$$\frac{dz}{dy}=\mp\frac{yR}{b^2}\left(1-\frac{y^2}{b^2}\right)^{-\frac{1}{2}} \tag{5}$$

$$\frac{d^2z}{dy^2} = \mp \frac{R}{b^2}\left(1-\frac{y^2}{b^2}\right)^{-\frac{1}{2}}\left(1-\frac{y}{b^2}\left(1-\frac{y^2}{b^2}\right)^{-1}\right) \tag{6}$$

The instantaneous radius of curvature with respect to the tool nose radius can be determined by substituting Eq. (5) and Eq. (6) into Eq. (2).

$$r' = \frac{1}{\rho} = \frac{\left[1+\frac{y^2R^2}{b^4}\left(1-\frac{y^2}{b^2}\right)^{-1}\right]^{\frac{3}{2}}}{\left|\frac{R}{b^2}\left(1-\frac{y^2}{b^2}\right)^{-\frac{1}{2}}\left(1-\frac{y}{b^2}\left(1-\frac{y^2}{b^2}\right)^{-1}\right)\right|} \tag{7}$$

At the lowest contact point ($y=0$), the tool nose radius of the wheel is given as:

$$\frac{1}{\rho} = \frac{b^2}{R} = r \tag{8}$$

$$b = \sqrt{Rr} \tag{9}$$

The final ellipsoid equation is denoted as:

$$\frac{x^2+z^2}{R^2} + \frac{y^2}{Rr} = 1 \tag{10}$$

2.2 Modelling of the 3D surface roughness profile

In grinding operation, forced vibration frequently arises due to the imbalance error of the wheel, which may be caused by inhomogeneous volume distribution, eccentric mounting or non-uniform wear of the wheel. These give rise to the fluctuations in the depth of cut as shown in Figure 2. The generation of surface roughness profile is directly associated with the relative motion between the grinding wheel and the workpiece. As a result, surface waviness is formed on the ground surface, which adversely affects the surface quality of the workpiece.

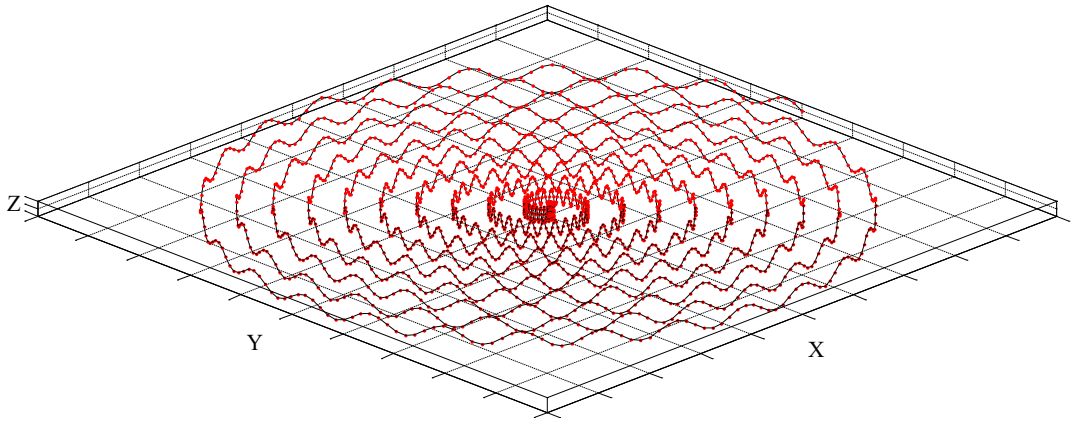

Fig. 2. Illustration of the locus of grinding wheel with micro-vibration

In the case of spinning spindles for both the grinding wheel and the workpiece, it is assumed that the wheel scratches the workpiece once during each cycle of revolution, where the grinding wheel travels a distance (uf) in the periphery of the workpiece. Meanwhile, the grinding wheel slides a radial distance (pf) towards the centre of the workpiece after the workpiece completes one revolution. The centre of the ellipsoid (X-Y plane) made by each cycle of revolution of the grinding wheel is shown as the dotted line in Figure 3.

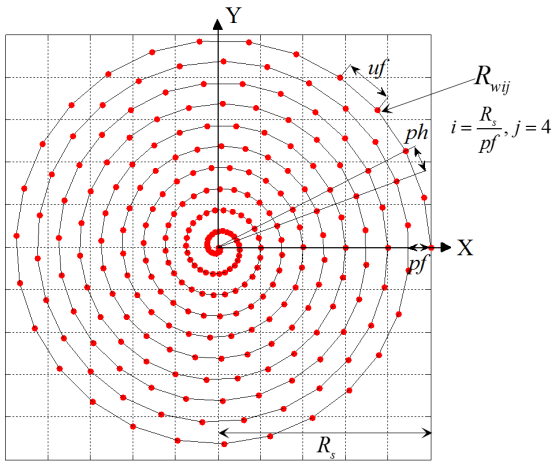

Fig. 3. The centre of the grinding wheel for each cycle in the X-Y plane

where N and ε are the integer part and decimal fraction of the speed ratio respectively, and it is derived as follows:

$$\frac{V_2}{V_1} = N \pm \varepsilon, \ -0.5 \le \varepsilon \le 0.5 \tag{11}$$

$$ph = 2\pi|\varepsilon| \tag{12}$$

$$pf = \frac{V_f}{V_1} \tag{13}$$

$$uf = \frac{2\pi V_1 R_p}{V_2} \tag{14}$$

where R_p is the distance between the grinding wheel and the rotary centre of the workpiece in the X-Y plane, and V_1 and V_2 are rotational speed of the workpiece and grinding wheel respectively.

It is assumed that the first cutting point is at the edge of the workpiece. The locus of ellipsoid centre can be determined as follows:

$$z = A\sin(2\pi V_2 \times \frac{R_p - \sqrt{x^2 + y^2}}{V_f}) \tag{15}$$

When grinding brittle materials, the depth of cut is extremely small so as to accomplish a good surface finish without fracture damage. It is assumed that the machined material is removed geometrically without considering the ploughing and crack phenomena in the final surface. The first cutting position is set at the perimeter of the workpiece (X-Z plane, Z=0).

The fluctuation of the grinding wheel with respect to the workpiece is assumed to be a simple harmonic motion with the rotational frequency of the grinding wheel and a small amplitude, as shown in Figure 4 (a) and 4 (b). As shown in Figure 4 (a), the fluctuation of the depth of cut for the grinding wheel leads to the phase shift and waviness formation and the ground surface exhibits different surface patterns at different phase shifts, as shown in Figure 4 (c) and 4 (d).

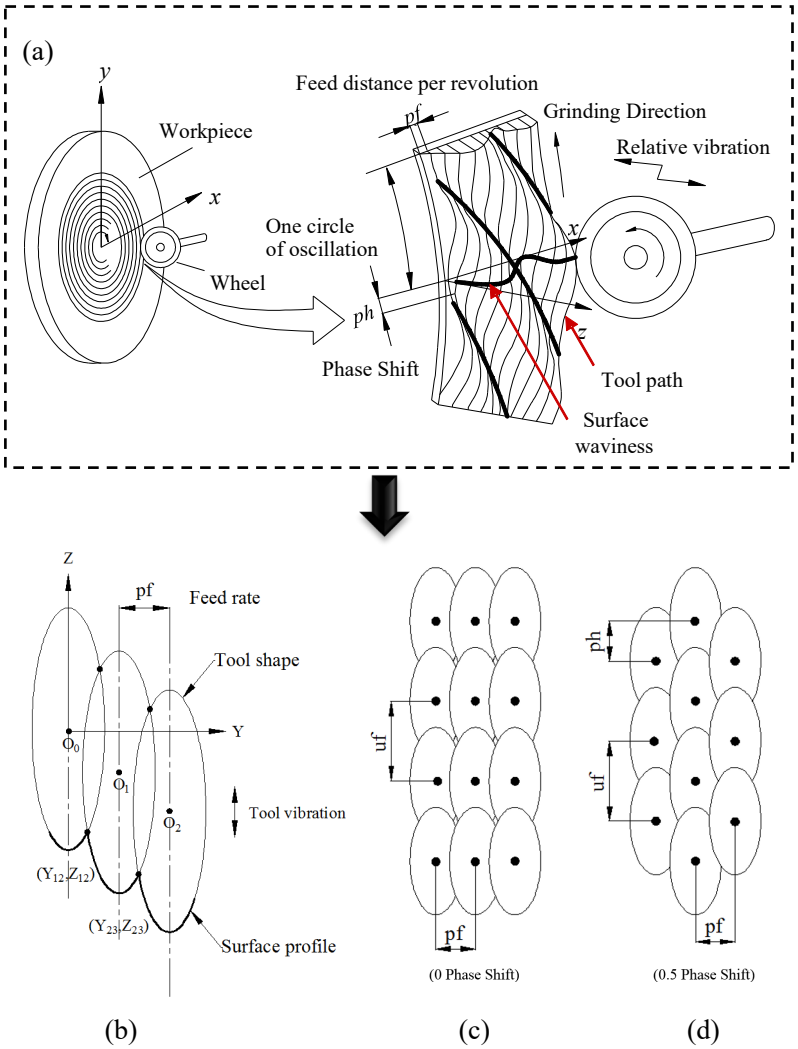

Fig. 4. Schematic diagram of the surface pattern generation in a radial direction: (a) surface generation mechanism, (b) the interference of a neighbouring cutting profile, (c) the surface generation with the phase shift 0, (d) the surface generation with the phase shift π (0.5)

In order to drive the tool profile intersection on the whole machined surface, a 2D surface profile is firstly calculated in the Z-Y plane (i.e. $X = 0$).

In the Z-Y plane, the cutting profile can be expressed as:

$$Z = -\sqrt{R^2 - \frac{Ry^2}{r}} \tag{16}$$

The relative displacement between the grinding wheel and the workpiece in the feed direction is:

$$Z_t = A\sin(\varphi\frac{y}{pf}) \tag{17}$$

The number of feed marks (N) is equal to $R_s \ / \ pf$, where R_s is the radius of the workpiece.

$$Z_t = A\sin[(i-1)\varphi],\ i = 1,2,...,N \tag{18}$$

The successive cutting tool profile is determined as:

$$Z(\mathrm{y}_i) = A\sin[(i-1)\varphi] - \sqrt{R^2 - \frac{R([y_i - (i-1)pf]^2}{r}} \tag{19}$$

$$Z(y_{i+1}) = A\sin(i\varphi) - \sqrt{R^2 - \frac{R(y_{i+1} - ipf)^2}{r}} \tag{20}$$

From Eq. (19) and Eq. (20), the intersecting point between the i th wheel profile and the $i+1$ th one can be solved as follows:

$$Z_{i,i+1} = \frac{r}{2}(B_i + B_{i+1}) - \sqrt{\frac{1}{4}(B_i + B_{i+1})^2 + \frac{r\Delta B_i^{\ 2} + R\Delta C_i^{\ 2}}{4r} - \frac{R\Delta C_i^{\ 2}(B_i^2 - \mathrm{R}^2)}{r\Delta B_i^{\ 2} + R\Delta C_i^{\ 2}}} \tag{21}$$

$$Y_{i,i+1} = \frac{-2r\Delta \mathrm{B}_i\, Z_{i,i+1} + r(\mathrm{B}_{i+1}^{\ 2} - \mathrm{B}_i^{\ 2}) - \mathrm{R}(C_i^{\ 2} - C_{i+1}^{\ 2})}{2R\Delta C_i} \tag{22}$$

where $B_i = A\sin[(\mathrm{i}-1)\varphi]$, $B_{i+1} = A\sin(i\varphi)$, $\Delta B_i = B_{i+1} - B_i$, $c_i = (i\text{-}1)pf$, $C_{i+1} = ipf$, $\Delta C_i = C_{i+1} - C_i$, $i = 1,2,\ldots,N-1$

Since the final machined surface is generated by the lowest region of the grinding wheel, the wheel profile above the intersection is removed. In order to determine the 3D surface topography, the workpiece surface is discretized according to a polar coordinate system in the X-Y plane.

The spiral locus of the grinding wheel is expressed within the polar coordinate system as:

$$\theta_i = i\Delta\theta,\ \ i = 0,1,2,...,N_s,\ \ N_s = \frac{2\pi}{\Delta\theta} \tag{23}$$

$$R_j = R_p - j\Delta r,\ \ j = 0,1,2,...,N_t, N_t = \frac{R_p}{pf} \tag{24}$$

In the X-Y plane, the corresponding coordinates for the locus of the tool centre are given as follows:

$$X_j = (R_p - j\Delta r)\sin(i\Delta\theta) \tag{25}$$

$$Y_j = (R_p - j\Delta r)\cos(i\Delta\theta) \tag{26}$$

$$Z_t(j) = A\sin(2\pi f_w \times \frac{j\Delta r}{V_f}) \tag{27}$$

The successive cutting tool profile is determined as:

$$Z(R_{wij}) = Z_t(j) - \sqrt{R^2 - \frac{R([j\Delta r - (j-1)pf]^2}{r}} \tag{28}$$

$$Z(R_{wi,j+n}) = Z_t(j+n) - \sqrt{R^2 - \frac{R[(j+n)\Delta r - (j+n-1)pf)^2}{r}} \tag{29}$$

where R_{wij} is defined in Figure 3.

At the $\theta_i = i\Delta\theta$ cross section, the intersection between two arbitrary ellipses can be determined as:

$$Z(r_{i,j,j+n}) = \frac{r}{2}[Z_t(j) + Z_t(j+n)] - \sqrt{\frac{1}{4}[Z_t(j) + Z_t(j+n)]^2 + \frac{r\Delta Z_t(j, j+n)^2 + Rn^2 pf^2}{4r} - \frac{Rn^2 pf^2 (Z_t(j)^2 - R^2)}{r\Delta Z_t(j, j+n)^2 + Rn^2 pf^2}} \tag{30}$$

$$r_{i,j,j+n} = \frac{-2r[Z_t(j) + Z_t(j+n)]Z(r_{i,j,j+n}) + r[Z_t(j+n)^2 - Z_t(j)^2] - Rpf^2(1 - 2j - 2n)}{2Rnpf} \tag{31}$$

Under a fine feed rate, it may have more than one intersection for the same point in the X-Y plane. As a result, the minimum value should be picked up, and the rest can be discarded.

2.3 Modelling and simulation of abrasive grains

In the process of surface generation, multitudinous abrasive grains with different protrusion heights and shapes interact with the workpiece in the cutting zone, which contribute to the surface generation. In order to establish the surface generation model in ultra-precision grinding, the cutting edges on the surface of the wheel need to be defined first. In the fabrication of the grinding wheel, a series of standard sieves are used to sort the grits (grit size screening) and the standard grit number is inverse to the grain size [30]. In general, each nominal grit size includes a range of grit sizes and its maximum diameter and the average diameter of the grit can be expressed in the following relationships [31]:

$$D_{g\max} = 15.2M^{-1} \tag{32}$$

$$D_{gavg} = 68M^{-1.4} \tag{33}$$

where M is the grit number.

Many studies have demonstrated that there exists a close correlation between protrusion height of the abrasive grain and grit size [31,32]. In addition, it is found that the majority of grinding wheel surfaces exhibit normal distribution characteristics [30]. The distribution of protrusion height for abrasive grain $h(z)$ can be expressed in Eq. (34). The expectation of the distribution μ, standard deviation σ and average grain interval Δ can be expressed as:

$$h(z) = \frac{1}{\sqrt{2\pi}\sigma}\exp\left(-\frac{(z-\mu)^2}{2\sigma^2}\right) \tag{34}$$

$$\mu = D_{gavg} \tag{35}$$

$$\sigma = \frac{1}{3}(D_{g\max} - D_{gavg}) \tag{36}$$

$$\Delta = D_{gavg}\sqrt[3]{\frac{25\pi}{3(32-S)}} \tag{37}$$

where S is the structural number of the wheel.

The abrasive grain G_i on the grinding wheel can be expressed as:

$$\begin{bmatrix} G_{ij}(x_{ij}) \\ G_{ij}(y_{ij}) \\ G_{ij}(z_{ij}) \end{bmatrix} = \left[R_{ij} + h(z_{ij}) \right] \times \begin{bmatrix} \sin\alpha_i \cos\beta_i \\ \sin\alpha_i \sin\beta_i \\ \cos\alpha_i \end{bmatrix} \qquad [\pi \le \alpha_i \le \pi],\ [0 \le \beta_i \le 2\pi] \tag{38}$$

where α_i is the angle between the z axis and vector R_{ij}

β_i is angle between the x axis and vector R_{ij}

The surface topography of the grinding wheel is generated by Eqs. (34) to (38). In this experiment, the grit number and the structural number of the wheel were chosen to be 500 and 7 respectively. Figure 5 shows the simulated surface topography of the grinding wheel by considering the wheel geometry. Figure 6 shows the wheel topography measured by an Alicona IFM Optical Measuring instrument. It is observed that the height of the abrasive grain basically follows the Gaussian distribution.

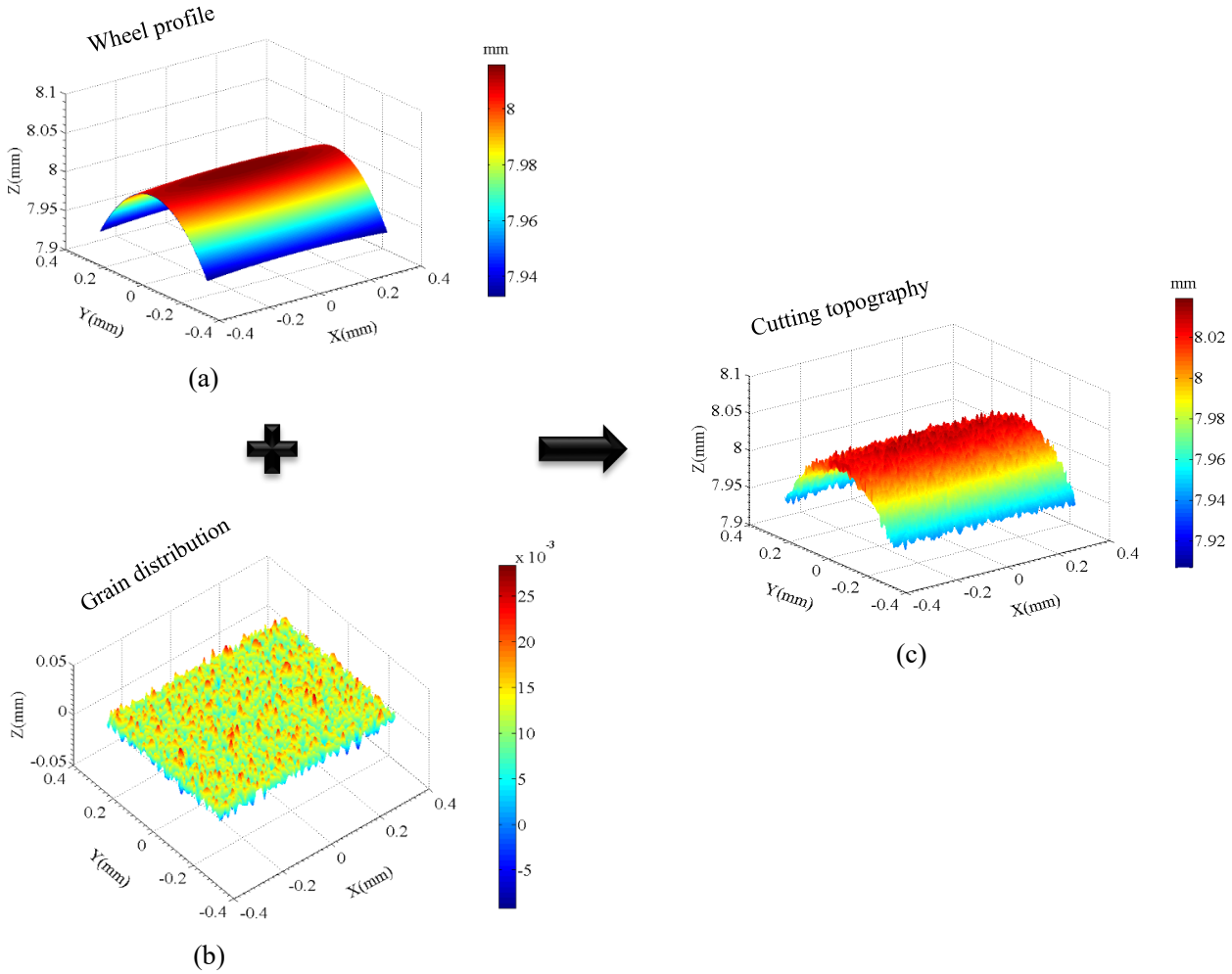

Fig. 5. Simulated 3D grinding wheel topography: (a) wheel profile, (b) grain distribution, (c) wheel topography

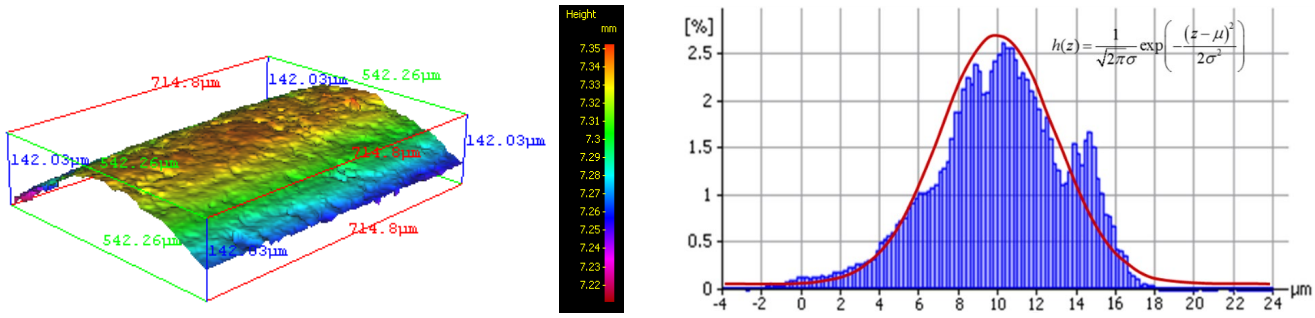

(a) (b)

Fig. 6. Measured grinding wheel surface: (a) surface topography (b) the distribution of protrusion height for abrasive grains

As shown in Figure 7, the grinding wheel travels along an Archimedean Spiral path (in the X-Y plane) from the edge region to the rotary centre of the workpiece. In polar coordinates (r, θ), the Archimedean Spiral can be expressed by Eq. (39), where a is the workpiece radius of the spiral and b controls the distance between neighbouring turnings.

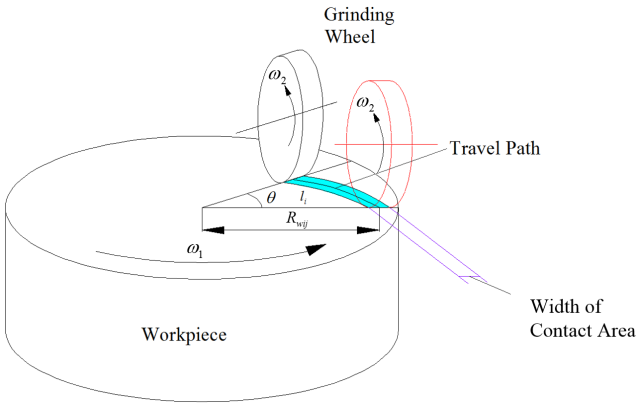

Fig. 7. The 2D map for the wheel locus in the X-Y plane

$$S_r = a + b\theta \quad (\mathrm{b} < 0), \qquad b = -\frac{V_f}{2\pi V_1} \tag{39}$$

The travel length for the wheel can be calculated by the following equations:

$$L_w(\theta) = \int_0^{\theta} \sqrt{S_r^{\,2} + \left(\frac{dS_r}{d\theta}\right)^2}\, d\theta \tag{40}$$

$$L_w(\theta) = \int_0^{\theta} \sqrt{(a+b)^2 + 2ab\theta + b^2\theta^2}\, d\theta \tag{41}$$

$$L_w(\theta) = \frac{2b^2\theta + 2ab}{4b^2}\sqrt{(a+b)^2 + 2ab\theta + b^2\theta^2} + \frac{b^2}{2}\int_0^{\theta} \frac{d\theta}{\sqrt{(a+b)^2 + 2ab\theta + b^2\theta^2}} \tag{42}$$

$$L_w(\theta)=\frac{2b^2\theta+2ab}{4b^2}\sqrt{(a+b)^2+2ab\theta+b^2\theta^2}+\frac{b^2}{2}\ln\left(\frac{b\theta+a}{b}+\sqrt{\left(\frac{b\theta+a}{b}\right)^2+1}\right) \tag{43}$$

In the grinding process, the final surface is generated by the sequential action of abrasive grains on the grinding wheel surface. The cumulative effect of abrasive grains' interference shapes the ground surface as shown in Figure 8.

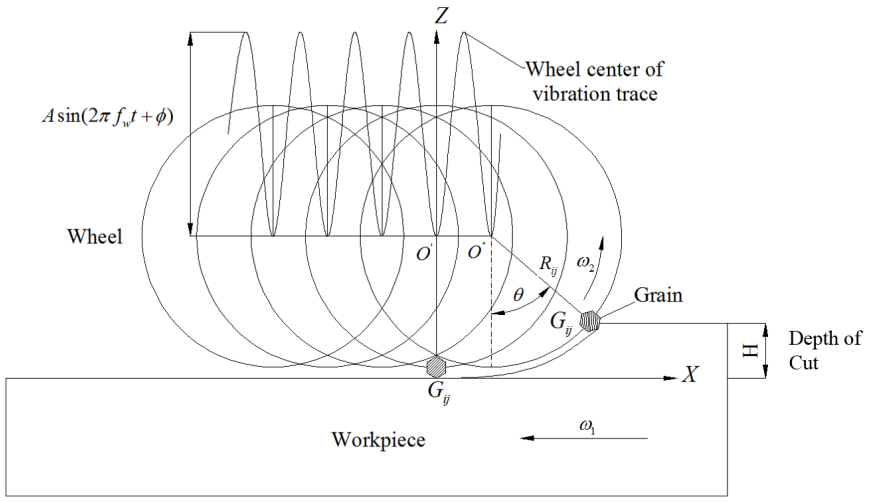

Fig. 8. Schematic of the abrasive trajectory with a micro oscillation

The cutting path of the grain G_{ij} can be expressed as:

$$x_{ij}=R_{ij}(\sin\theta+\frac{R_{wij}\omega_1}{R_{ij}\omega_2}\theta) \tag{44}$$

where R_{wij} is the distance between the contact point (G_{ij}) and the machined centre in the X-Y plane.

x_{ij} is the arc length of an abrasive grain traversing the workpiece.

$$z_{ij}=R_{ij}(1-\cos\theta) \tag{45}$$

Since θ is very small, Eqs. (44) and (45) can be approximately revised as:

$$z_{ij}=\frac{R_{ij}x^2}{2(R_{ij}+\frac{R_{wij}\omega_1}{\omega_2})^2} \tag{46}$$

The micro-vibration of the grinding wheel generates an extra displacement, which usually appears in the form of a sinewave [30-32]. As a result, the trace of the G_{11} can approximated by Eq. (47):

$$z=\frac{R_{11}x^2}{2(R_{11}+\frac{R_{w11}\omega_1}{\omega_2})^2}+A\sin(2\pi f_w t_0+\phi) \tag{47}$$

Similarly, the trajectory for the grain G_{1j+1}, can be expressed as:

$$z=\frac{R_{1j}\left(x-L_w[(j-1)\frac{2\pi\omega_2}{N_G\omega_1}]\right)^2}{2(R_{1j}+\frac{R_{w1j}\omega_2}{\omega_1})^2}+A\sin\left[2\pi f_w\left[t_0+(j-1)\Delta t\right]+\phi\right]+R_{11}-R_{1j} \tag{48}$$

$$L_w((j-1)\frac{2\pi\omega_2}{N_G\omega_1})=\frac{2b^2(j-1)\frac{2\pi\omega_2}{N_G\omega_1}+2ab}{4b^2}\sqrt{(a+b)^2+2ab(j-1)\frac{2\pi\omega_2}{N_G\omega_1}+b^2[(j-1)\frac{2\pi\omega_2}{N_G\omega_1}]^2} + \frac{b^2}{2}\ln\left(\frac{b(j-1)\frac{2\pi\omega_2}{N_G\omega_1}+a}{b}+\sqrt{\left(\frac{b(j-1)\frac{2\pi\omega_2}{N_G\omega_1}+a}{b}\right)^2+1}\right) \tag{49}$$

where N_G is the total number of abrasive grains in one circle.

According to Eqs. (1) to (31), the intersection of adjacent wheel profiles can be determined and the effective contact area between the grinding wheel and workpiece in each path can be obtained accordingly. The abrasive within the effective cutting region on the wheel surface is modelled to determine the 3D ground surface topography. As a result, the final ground surface contains both surface roughness and surface waviness. As shown in Figure 9, the iterating interference of neighbouring grit trajectories results in the final surface generation, in which the subsequent lower cutting path of abrasive grains will replace the previous path and finally the lowest cutting path contributes to the surface generation. In order to simulate the grit's motion, the workpiece surface is discretized along the cutting direction. The path of each grit can be determined according to Eqs. (44) to (49) and the lowest location $(Z_{ij}, \mathrm{X}_{ij})$ of the cutting path at each discrete point of the workpiece can be obtained by Eq. (50).

$$Z_{ij}(X_{ij})=\min[Z_{1j}(X_{ij}),Z_{2j}(X_{ij}),Z_{3j}(X_{ij}),...Z_{n-1j}(X_{ij}),Z_{nj}(X_{ij})] \tag{50}$$

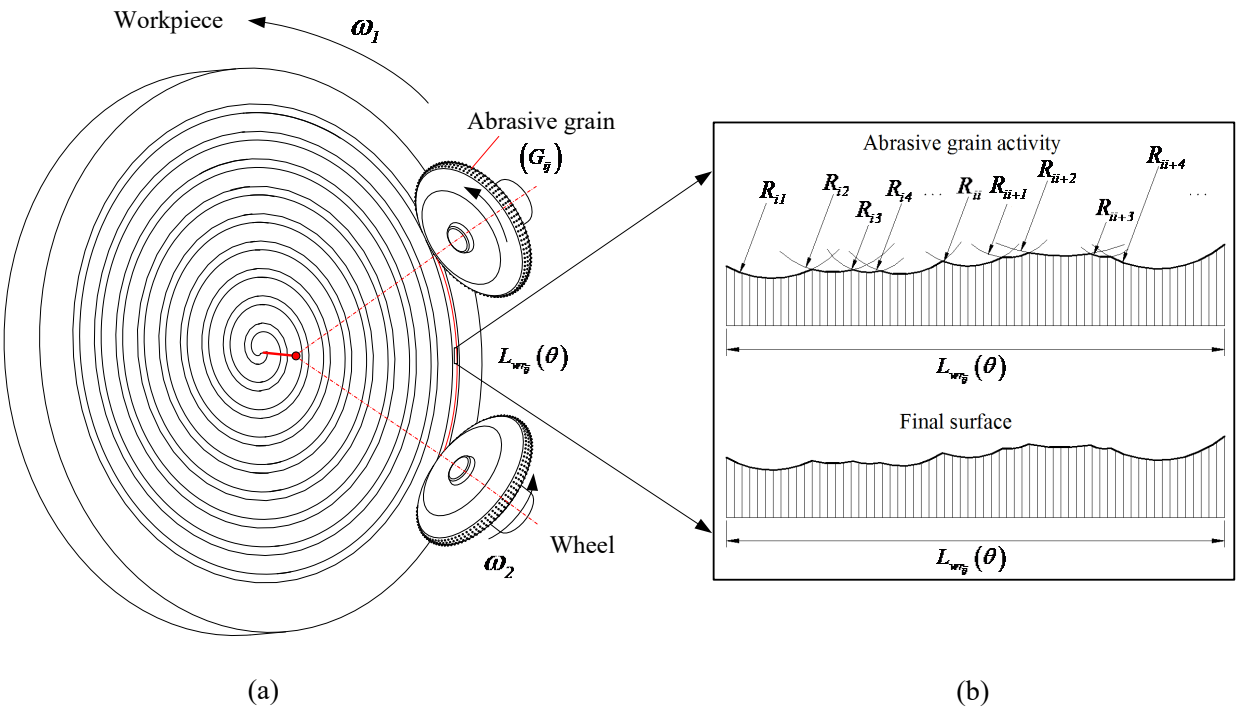

(a) (b)

Fig. 9. Surface generation process in grinding: (a) grinding path, (b) interference of abrasive grains and surface generation

3 Phase Simulation and Experimental Verification

3.1 Design and Setup of the Experiments

To verify the theoretical model of surface generation in ultra-precision grinding, a series of grinding experiments was conducted on a Moore Nanotech 450UPL ultra-precision grinding machine. This machine can be used to perform ultra-precision micro-grinding of optical materials as shown in Figure 10. A grinding wheel moves in one direction (Z axis) with a rotary axis (i.e. B axis). The workpiece is mounted by a vacuum chuck which moves along the X axis (i.e. cross feed). The wheel diameter and thickness are 16 mm and 5 mm respectively with an arc (nose radius 0.5 mm) in the cutting edge. The grinding conditions and mechanical properties of SiC are summarized in Table 1 and Table 2, respectively.

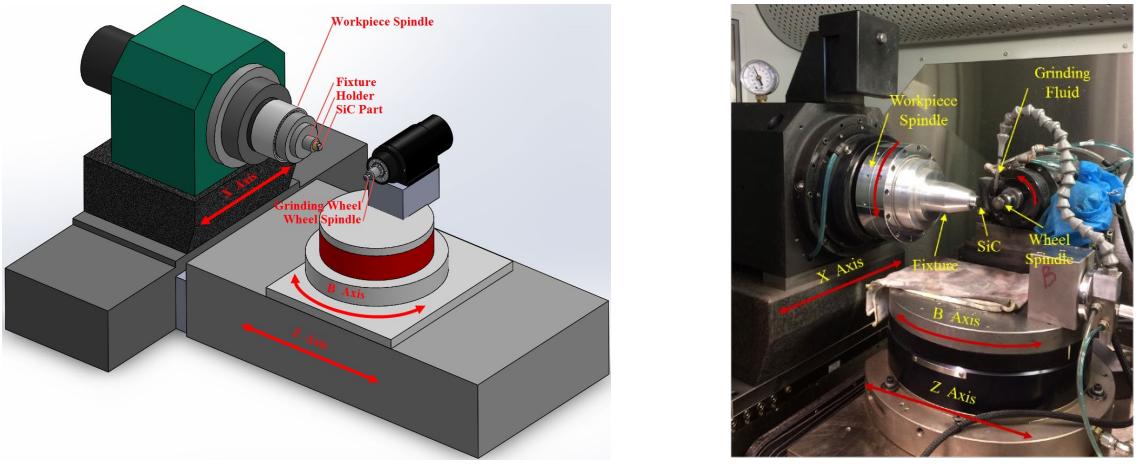

(a) (b)

Fig. 10. Schematic diagram of the grinding machine: (a) configuration of the machine, (b) layout of the tool spindle

Table 1 Grinding wheel and grinding parameters

Grinding Wheel	Resin bonded diamond wheel: 500-grit, diameter: 16 mm, thickness: 5 mm, nose radius: 0.5 mm
Speed of the grinding wheel (V_2) (RPM)	39000-40500
Speed of the workpiece (V_1)(RPM)	1500
Feed rate (V_f) (mm per min)	10
Depth of cut (μm)	10
Dresser and Truer	Single diamond nib and aluminium oxide stick
Coolant	CLAIRSOL 330

Table 2 Material properties of SiC

Workpiece	Reaction Bonded SiC
Compressive strength (MPa)	2000
Young's modulus (H) (GPa)	410
Vickers hardness (H_v) (GPa)	2500
Fracture toughness (K_{IC}) (MPa·m^{½})	4.0
Density (g/cm^3)	3.1
Dimension	9 mm × 9 mm × 5 mm

Since the shape and the surface topography of the wheel have a direct effect on the machined surface tolerances and surface quality, dressing and truing of the wheel are very important to decide the grinding preference. In order to keep the same cutting profiles for all the tests, the grinding wheel was firstly dressed and trued with the same cutting parameters before each experiment. The dressing and truing conditions are shown in Table 3. After the end of grinding, a Zygo Laser Interferometric Non-contact Profiler was used to measure the profile of the machined surface.

Table 3 Wheel dressing and truing conditions

Items	Operation parameters		
	Rotational speed (RPM)	Feed rate (mm/min)	Depth of cut (μm)
Wheel dresser	300	2	5
Wheel truer	500	0.5	2
Grinding wheel	2000	0.5	1
Coolant	CLAIRSOL 330		

3.2 Simulation results for the phase shift effect

During grinding, in order to make a changeable fractional part (0,0.1,…1) for the speed ratio between the grinding wheel and the workpiece, the rotational speed of the grinding wheel was increased from 39000 RPM to 40500 RPM with a 150 RPM interval, and the workpiece speed was kept constant at 1500 RPM in all experiments. The phase shift (ph) can be determined by Eq. (12). Due to fine feed rate ($pf = 6.7\mu m$), a minimal phase shift can accumulate over many cycles

on the ground surface, which is able to significantly distortion of the surface patterns. In high-speed grinding, the rotational speed of the wheel cannot remain perfect; instead, there is a very slight error (about 0.05% of the wheel speed). It was found that the average speed for the grinding wheel was about 18 RPM larger than the preset speed by recording 10 speed values for each test. To obtain the vibration amplitude (A), an ultra-high-speed and high-accuracy laser displacement sensor was employed to achieve the vibration amplitude of the grinding wheel. It was found that the variation of surface height of the grinding wheel was approximatively 2.5 μm for all rotational speeds of the grinding wheel in the range between 39000 RPM and 40500 RPM. Figure 11 shows a typical relative displacement signal with a 0.5 μs sampling interval.

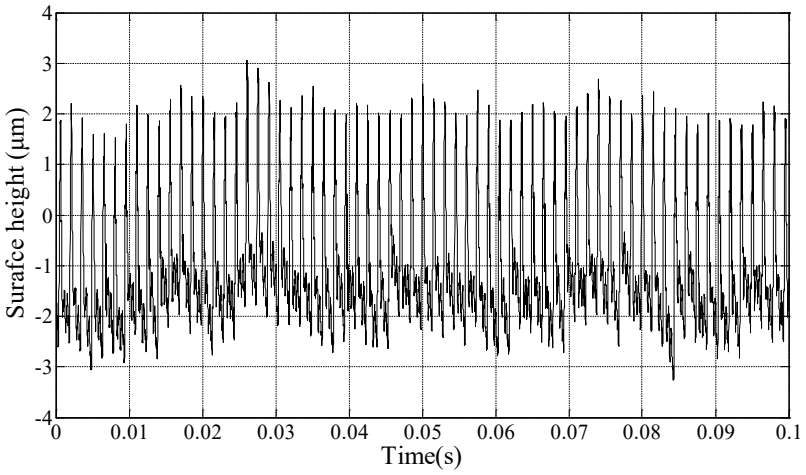

Fig. 11. Graph of the measured relative error motion of the grinding wheel

Figure 12 shows a comparison of the simulation and experimental results. It is interesting to note that the simulated roughness profiles agree reasonably well with that of measured surface patterns. The integer speed ratio leads to a light superimposition for the wheel profile in a 3-D space, which contributes to the deeper scratches, such as simulated results 12.a (1), 12.a (11) and measured results 12.b (1), 12.b (11). In addition, there are three main surface features on the machined surfaces including feed marks (pf), imbalanced vibration and phase shift marks. For feed marks, there is a spiral pattern from the edge area to machined centre, which represents the tool locus and tool geometry. Chatter vibration associated with the imbalanced wheel posed a series of surface waviness on the ground surface the geometry of which is governed by the grinding parameters. Phase shift marks associated with waviness shift are caused by phase accumulation. The phase shift marks are not obvious when the phase is near to 0 or 1, which is submerged by the chatter waviness, as shown in 12.a (1), 12.a (2), 12.a (10), 12.a (11). Abrasive marks further trim the waviness profile, leading to inhomogeneous ground surface. With an increase of the phase shift from 0 to 0.4, the density of the grinding marks increases but the marks' density decreases significantly when the phase shift is equal to 0.5. Since the nose radius of the wheel $(r = 0.5 \ \ mm)$ is much larger than the feed rate $(pf = 1/150 \ \ mm)$, it appears that there are fewer cuts for the tool engagement marks in the same area than those of the phase shift at 0.4 and 0.6 , as shown in Figure 12.a (5)-a (7) and 12.b (5)-b (7).

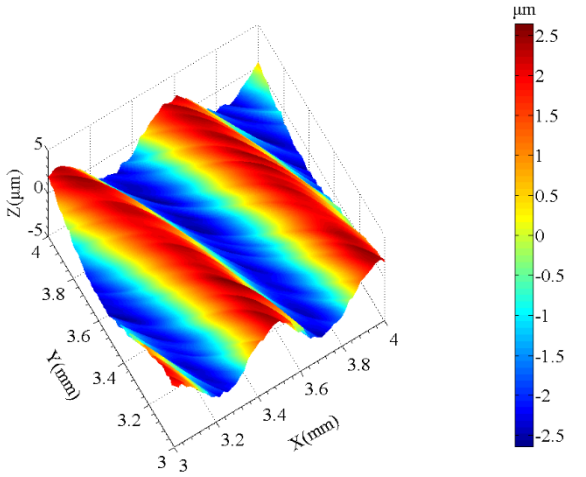

a (1)

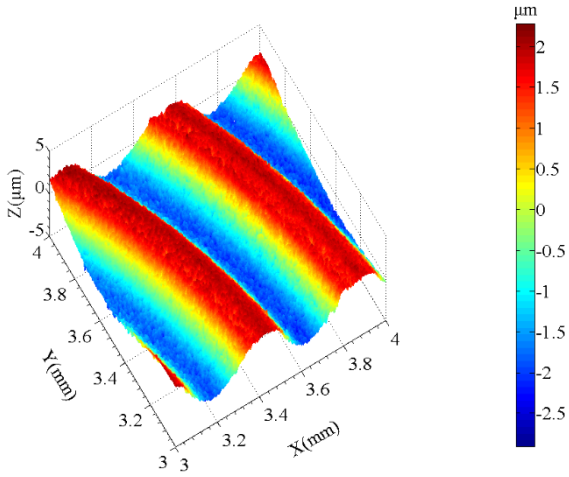

b (1)

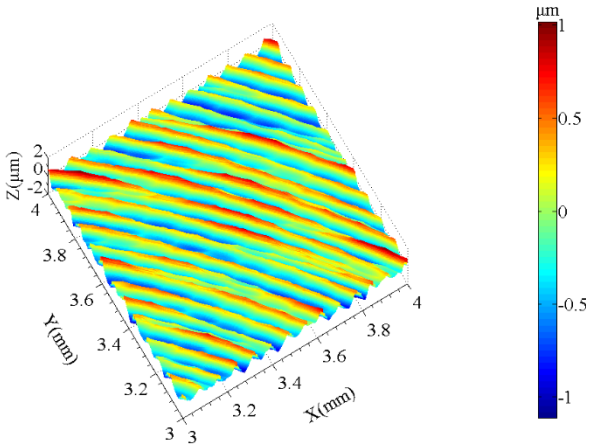

a (2)

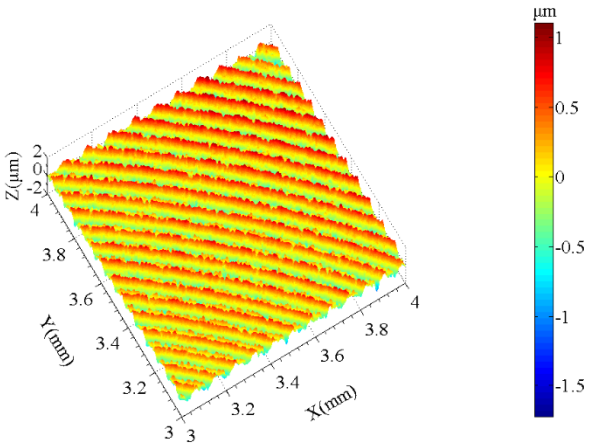

b (2)

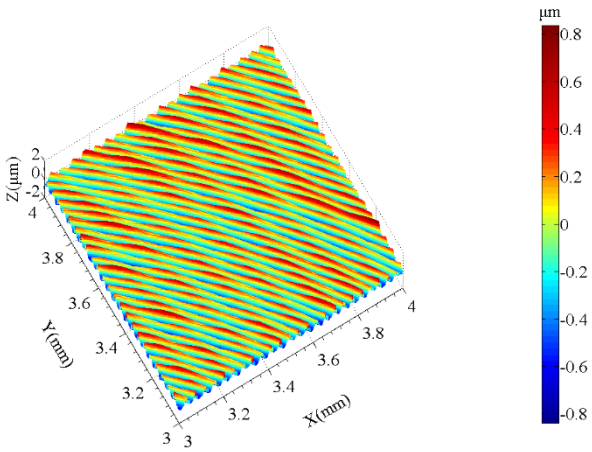

a (3)

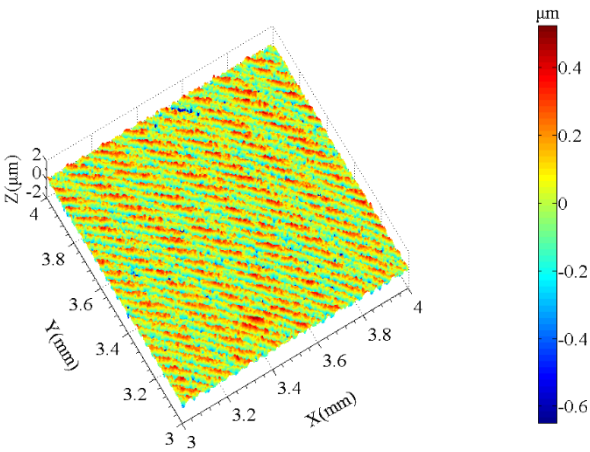

b (3)

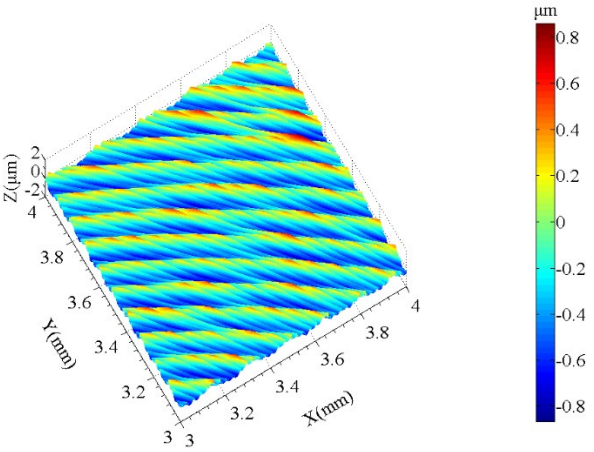

a (4)

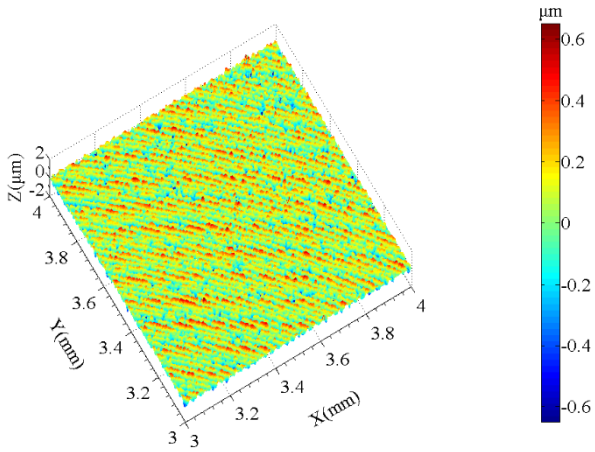

b (4)

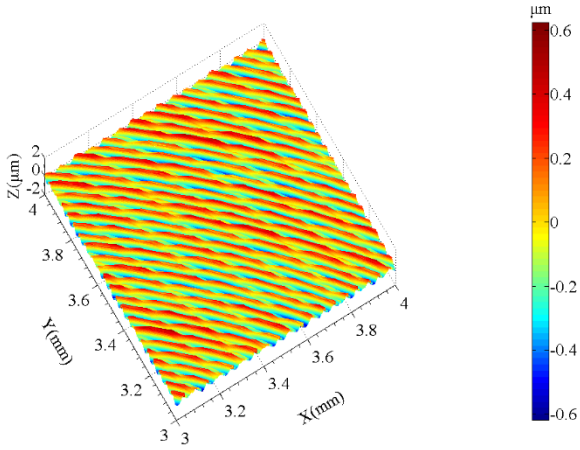

a (5)

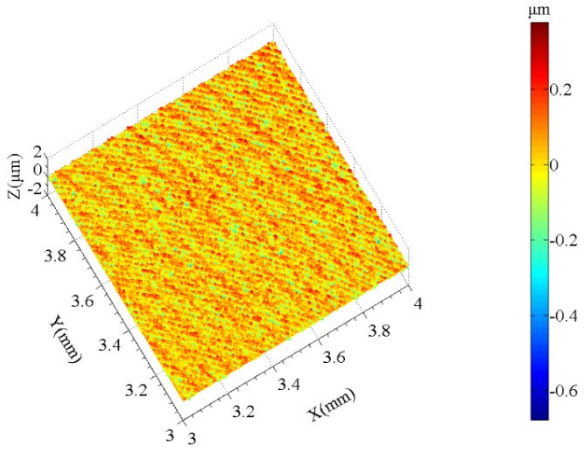

b (5)

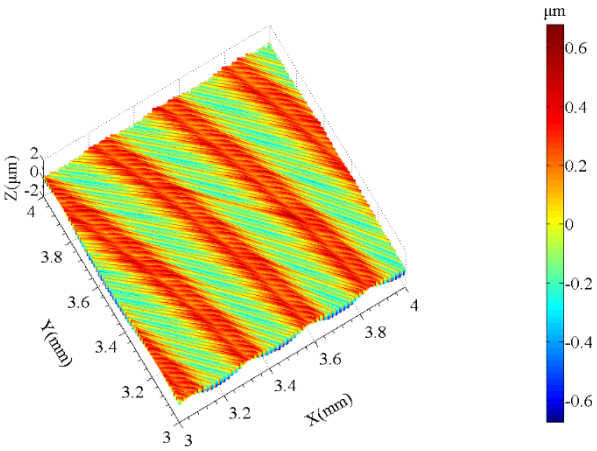

a (6)

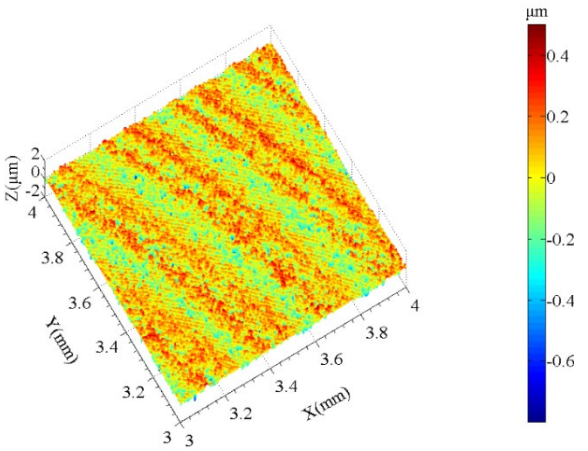

b (6)

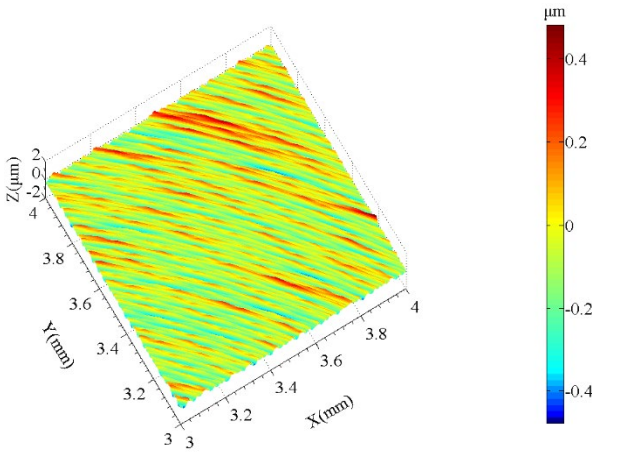

a (7)

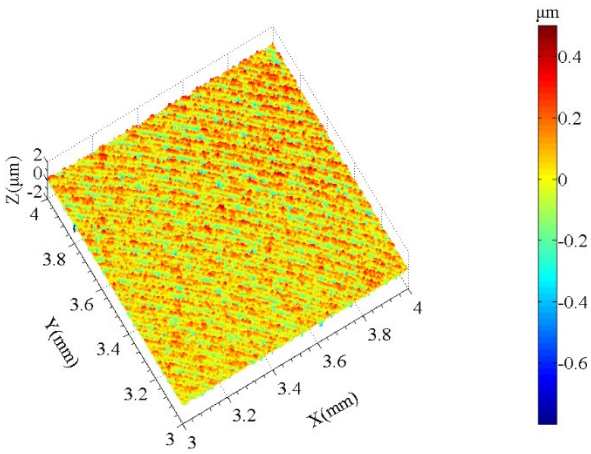

b (7)

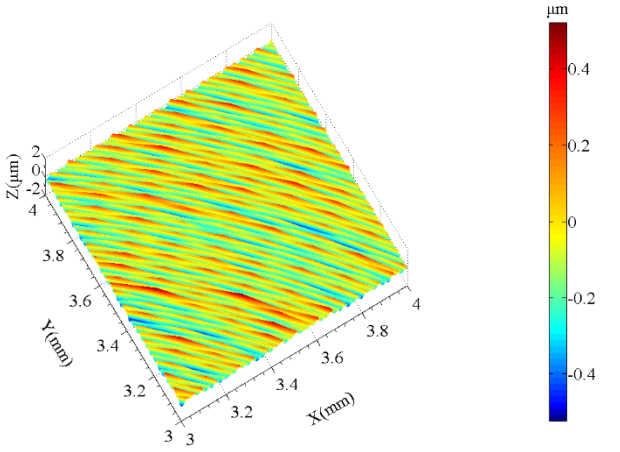

a (8)

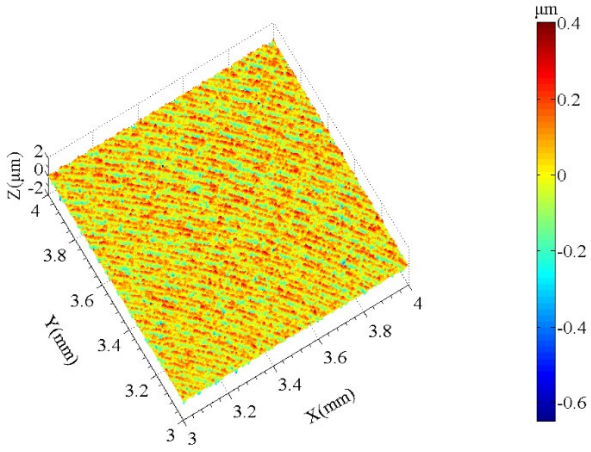

b (8)

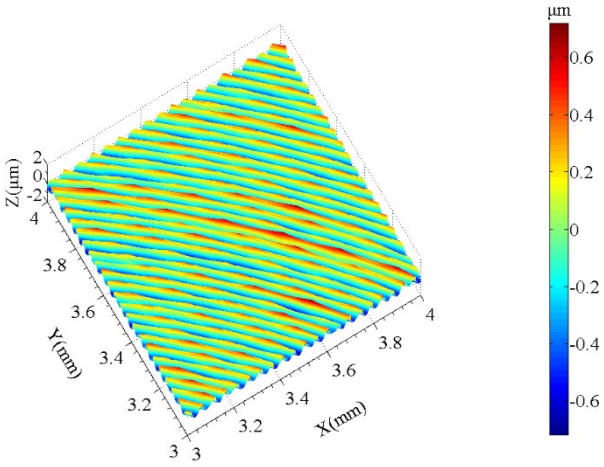

a (9)

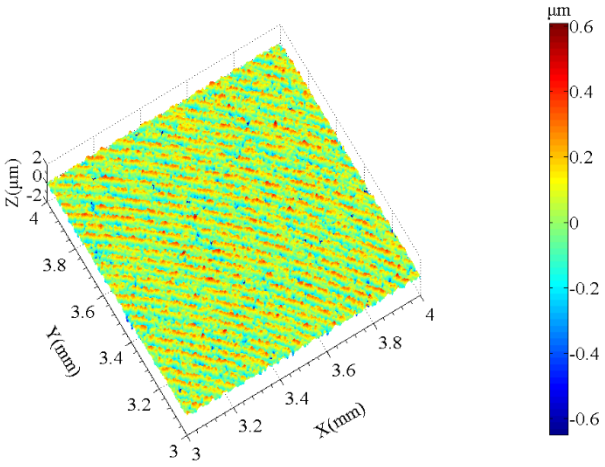

b (9)

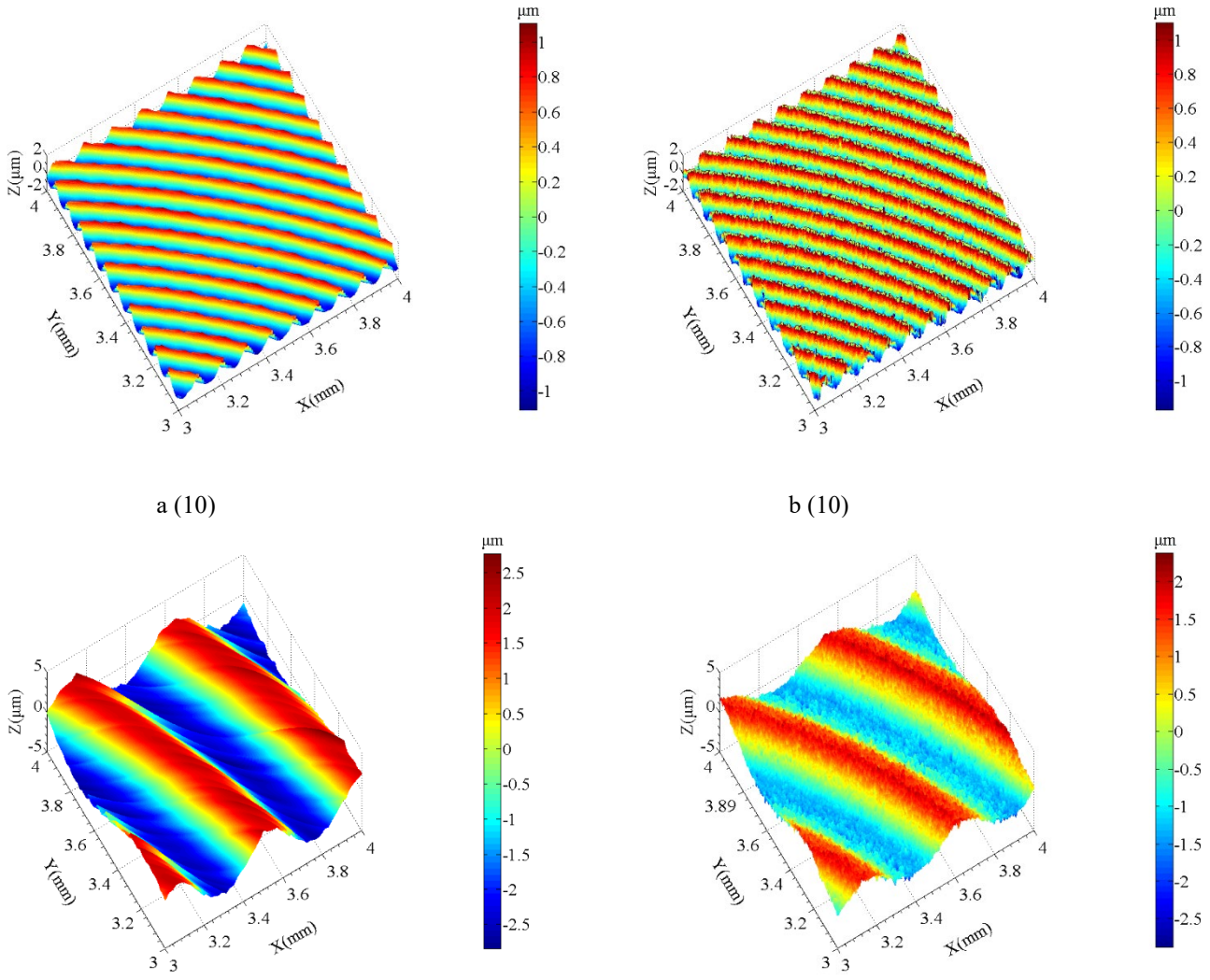

a (10) b (10)

a (11) b (11)

Fig. 12. Simulated surface topographies a (1)-a (11) and measured surface topographies b (1)-b (11) under changeable phase shift (0,0.1…1.0) respectively; rotational speed of the wheel: 39000-40500 RPM, feed rate: 10 mm per min, depth of cut: 10 μm , rotational speed of the workpiece: 1500 RPM

To further verify the surface generation model quantitatively, the measured data and simulated surface have to be accurately transferred to the same coordinate by spatial translation and rotation so as to make the two surfaces match closely [33,34]. In this research, the iterative closest point (ICP) was chosen to match the theoretical and measured surfaces for the calculation of an optical transformation matrix; then the error map representing the deviation of corresponding points between simulated and measured data can be determined. Figure 13 shows the matching process of simulated and measured surfaces for the case in Figure 12 a (1) and Figure 12 b (1). It was found that the simulated surface topography agrees with the measured surfaces well for different phase shifts as shown in Figure 14. Figure 15 shows the root-mean-squared value (RMS) of the matching errors, which reflects the prediction accuracy of the surface generation model. It was found that the RMS ranges from 0.15 μm to 0.5 μm . This further shows that the simulated surface topographies are in good agreement

with the experimental results.

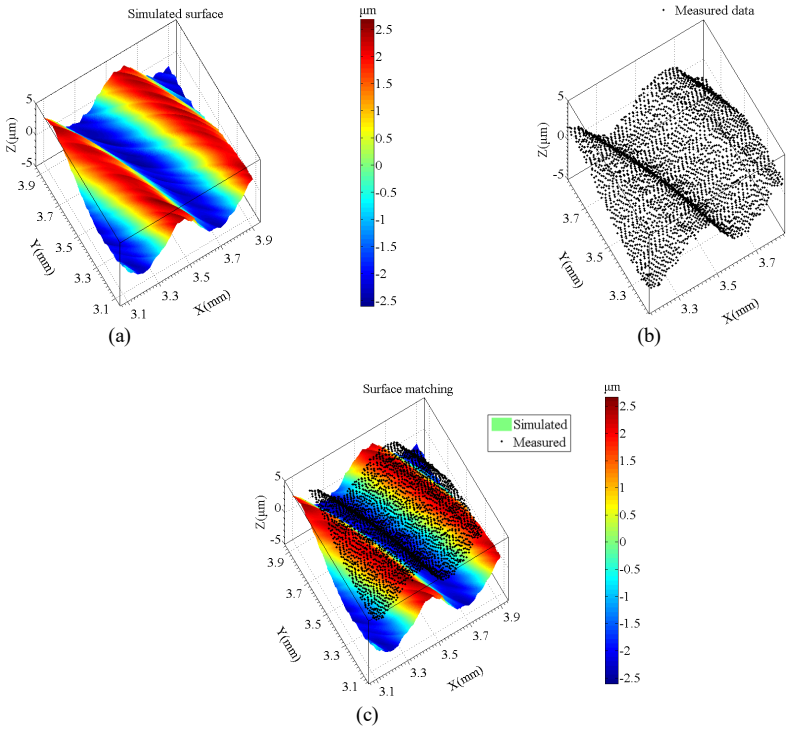

Fig. 13. Surface matching process for case 12 a (1) and 12 b (1) in Figure 12. (a) Simulated surface, (b) Measured surface, (c) Surface matching result

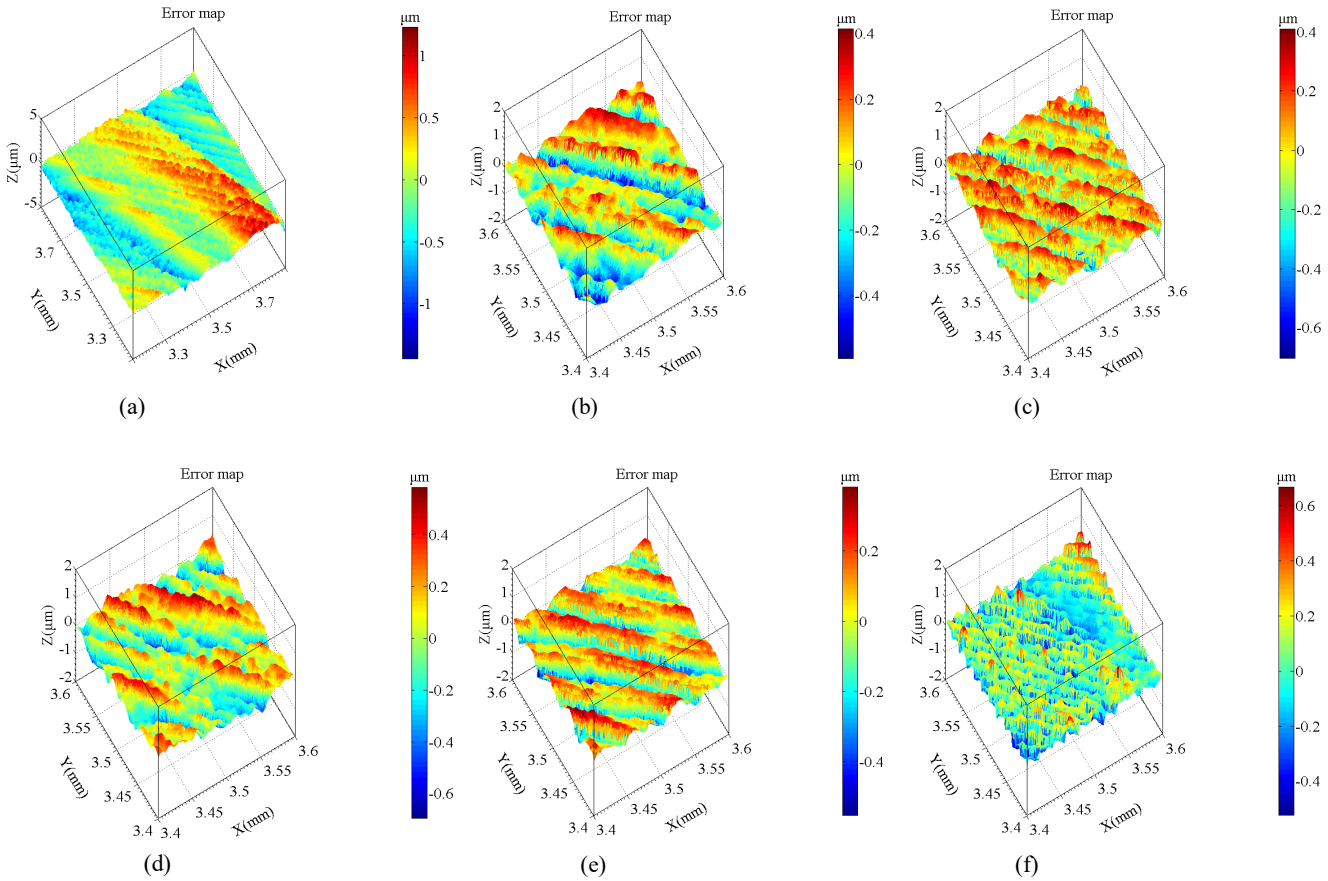

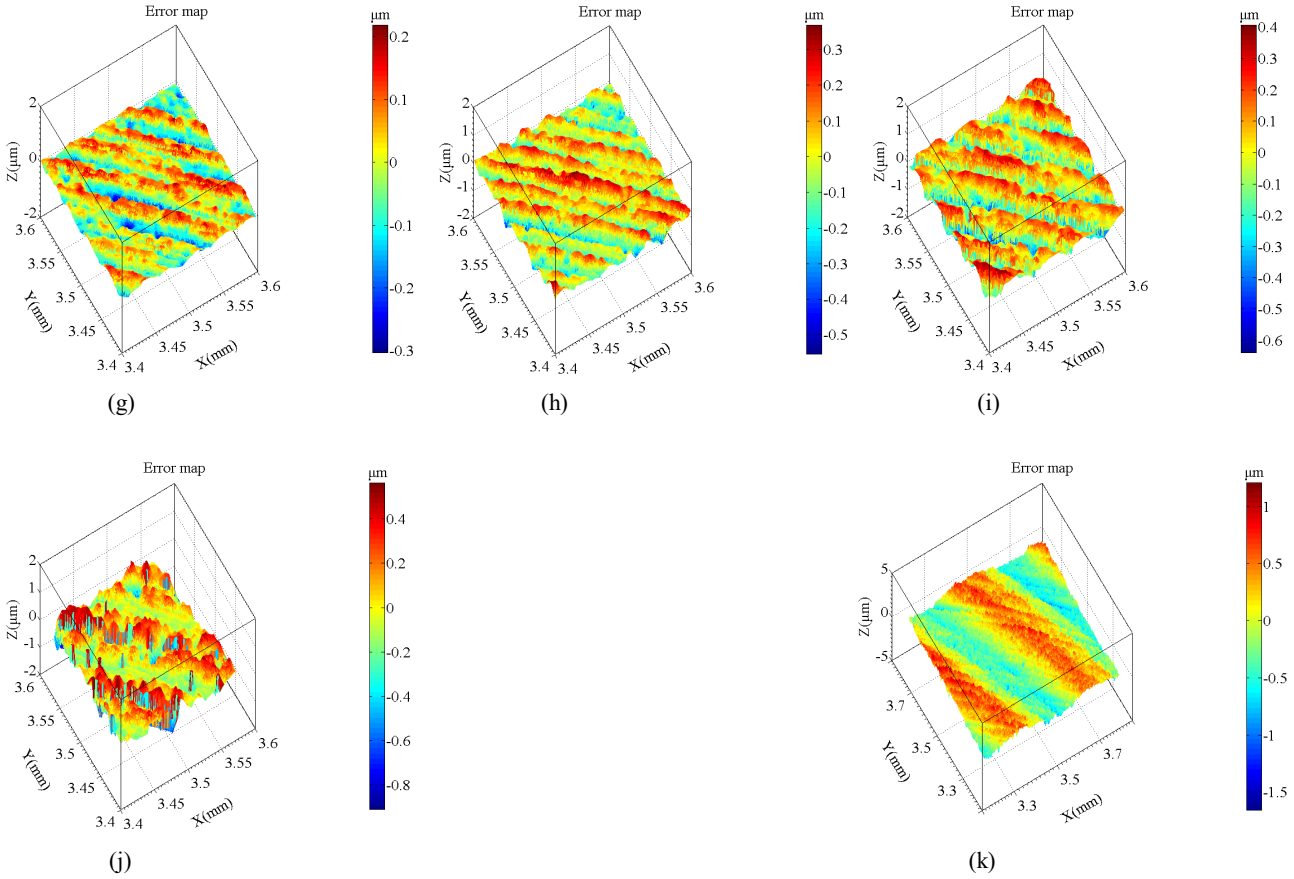

Fig. 14. Evaluated matching error map of ground surface for different phase shifts in grinding RB-SiC

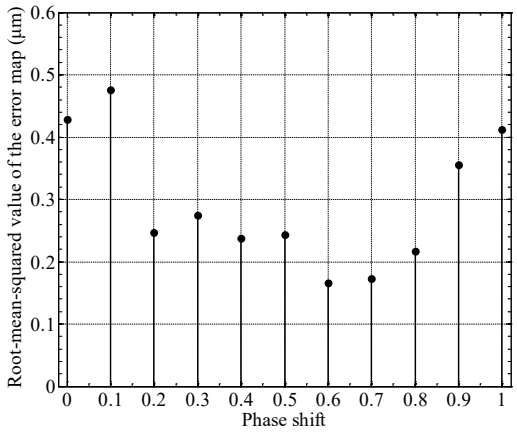

Fig. 15. The root-mean-squared value of the matching error maps

4 Conclusions

In this study, the modelling and simulation of surface generation in ultra-precision grinding were undertaken. A three-dimensional theoretical model was built to describe the interaction between the grinding wheel and workpiece. The model takes into account the micro-vibration of the grinding wheel, phase shift, grinding kinematics, wheel geometry and random distribution of the abrasive grit protrusion heights. It helps to reveal the evolution mechanism of surface generation.

It is shown that the phase shift is the critical influential factor in surface generation in ultra-precision grinding. As the phase shift increases from 0 to 0.4, the density of the spiral pattern increases. However, the middle phase shift (0.5) undergoes a remarkable decrease, which is caused by the fine feed rate with respect to the tool nose radius. For small change of rotational speed of the grinding wheel (i.e. from 39000 RPM to 39150 RPM), the ground surfaces have considerably different patterns.

In addition, four main grinding marks were found on the machined surface: spirals, tool feed marks, vibration marks and grain scratches. The surface matching process further verifies that the 3D theoretical model for surface generation agrees reasonably well with the experimental results. Hence, the 3D model can be used to predict surface generation in the grinding of brittle materials and give an insight into the ultra-precision grinding process.

Acknowledgments

The work was supported by a PhD studentship (project account code: RU3K) and a MPhil studentship (project account code: RU7J) from The Hong Kong Polytechnic University. This research work was also supported by the State Key Basic Research and Development Program, China (973 program, Grant no. 2011CB 013202) and Guangdong Provincial Department of Science and Technology, Guangdong, P.R. China for The Introduction of Innovative R&D Team Program of Guangdong Province (Project no.:201001G0104781202).

References

[1] S. Malkin, T. W. Hwang, Grinding mechanics for ceramics, Annals of the CIRP, 45(2) (1996), pp. 569-580.

[2] C. Chen, Y. Jung, I. Inasaki, Surface, Cylindrical and internal grinding of advanced ceramics: grinding fundamentals and applications, ASME Journal of Manufacturing Science and Engineering, 39 (1989), pp. 201-211.

[3] J. Cheng , Y. D. Gong, Experimental study of surface generation and force Modelling in micro-grinding of single crystal silicon considering crystallographic effects, International Journal of Machine Tools and Manufacture, 77 (2014), pp. 1-15.

[4] R. L. Allor, S. Jahanmir, Current problems and future directions for ceramic machining, American Ceramic Society Bulletin, 75(7) (1996), pp.40-43.

[5] B. Bhattachcharya, Ductile regime nano-machining of Silicon carbide, Master's Thesis, Western Michigan University,2005.

[6] S. Ito, M. Nakamura, W. Kanematsu, Machining of high performance ceramics. Bulletin of the Japan Society of Precision Engineering, 21(3) (1987), pp.167-172.

[7] H. Kiso, T.Taguchi, M. Fukuhara, T. Kimura, Machining of advanced ceramics by turning with sintered polycrystalline diamond tool, Bulletin of the Japan Society of Precision Engineering, 21(2) (1987), pp.142-143.

[8] H. Kasuga, H. Ohmori, T. Mishimal, Y. Watanabe, W. Lin, Investigation on mirror surface grinding characteristics of SiC materials, Ceramic Processing Research, 10(3) (2009), pp.351-354.

[9] A. Thomas, B. Georg, Application of atmospheric plasma jet machining (PJM) for effective surface figuring of SiC. Precision Engineering, 36(4)

(2012), pp.546-553.

[10] J. H. Zhang, Y. M. Zhang, J. C. Han, X. D. He, W. Yao,Design, fabrication and testing of space-borne SiC mirror, Optics and Precision Engineering, 14(2) (2006), pp.179-184.

[11] D. H. Zhu, S. J. Yan, B. Z. Li, Single-grit Modelling and simulation of crack initiation and propagation in SiC grinding using maximum undeformed chip thickness,Computational Materials Science, 92 (2014), pp.13-21.

[12] M. A. Ealey, G. Q. Weaver, Developmental history and trends for reaction bonded silicon carbide mirrors, SPIE proceeding, 2857 (1996), pp.66–72.

[13] J. Gao, J. Chen, G. Liu, Y. Yan, X. Liu, Z. Huang, Role of microstructure on surface and subsurface damage of sintered silicon carbide during grinding and polishing, Wear, 270 (2010), pp.88-94.

[14] J. M. Boettger, Effect of grinding wheel sharpness on the microstructure and surface finish of hardened and tempered 52100 steel, The University of Connecticut, Master thesis, 1995.

[15] S. Agarwal, P. V. Rao, Modelling and prediction of surface roughness in ceramic grinding, International Journal of Machine Tools and Manufacture, 50(12) (2010), pp.1065-1076.

[16] R. L. Hecker , S. Y. Liang, Predictive Modelling of surface roughness in grinding, International Journal of Machine Tools and Manufacture, 43(8) (2003), pp.755-761.

[17] J. L. Jiang , P. Q. Ge, J. Hong, Study on micro-interacting mechanism Modelling in grinding process and ground surface roughness prediction, The International Journal of Advanced Manufacturing Technology, 67 (2013), pp.1035-1052.

[18] D. Pal, A. Bangar, R.Sharma, A. Yadav, Optimization of grinding parameters for minimum surface roughness by Taguchi parametric optimization Technique, Mechanical and Industrial Engineering, 1(3) (2012), pp.74-78.

[19] C. H. Lee, Y. Shin, Evolutionary modelling and optimization of grinding processes, International Journal of Production Research, 38(12) (2000), pp.2787-2813.

[20] H. K. Tonshoff, B. Karpuschewski, T. Mandrysch, Grinding process achievements and their consequences on machine tools challenges and opportunities, Annals of the CIRP, 47 (1998), pp.651-668.

[21] L. Blunt, S. Ebdon, The application of three-dimensional surface measurement techniques to characterizing grinding wheel topography, International Journal of Machine Tools and Manufacturing, 36(11) (1996), pp.1207-1226.

[22] T. W. Hwang, C. J. Evens, S. Malkin, High speed grinding of silicon nitride with electroplated diamond wheels, part 1: wear and wheel Life, ASME Journal of Manufacturing Science and Engineering, 121(1) (1999), pp.32-41.

[23] P. Puerto, R. Fernández, J. Madariaga, J. Arana, I. Gallego, Evolution of surface roughness in grinding and its relationship with the dressing parameters and the radial wear, Procedia Engineering, 63 (2013), pp.174-182.

[24] J. Cheng, Y. D. Gong, J.S Wang, Modelling and evaluating of surface roughness prediction in micro-grinding on soda-lime glass considering tool characterization, Chinese Journal of Mechanical Engineering, 26(6) (2013), pp.1091-1100.

[25] Y.M. Liu, A. Warkentinb, R. Bauerb, Y.D Gong, Investigation of different grain shapes and dressing to predict surface roughness in grinding using kinematic simulations, Precision Engineering, 37 (2013), pp.758-764.

[26] A. McDonald, A. M. O. Mohamed, .A.Warkentin, .R. J. Bauer, Kinematic simulation of the uncut chip thickness and surface finish using a reduced set of 3D grinding wheel measurements, Precision Engineering, 49 (2017), pp.169-178.

[27] I. Aleksandrova, Optimization of the dressing parameters in cylindrical grinding based on a generalized utility function, Chinese Journal of Mechanical Engineering, 29(1) (2016), pp.63–73.

[28] T. Kuriyagawa, N. Yoshihara, M. Saeki, K. Syoji, Nano-topography characterization of axisymmetric aspherical ground surfaces, Key Engineering Materials, 238–239 (2003), pp.125–130.

[29] N. Yoshihara, J. W Yan, T. Kuriyagawa, Control of nano-topography on an axisymmetric ground surface, Key Engineering Materials, 389-390 (2009),

pp.96-101.

[30] Y. L. Cao, J. Y. Guan, B. Li, X. L. Chen, J. G. Yang, C. B. Gan, Modelling and simulation of grinding surface topography considering wheel vibration, Advanced Manufacture Technology, 66 (2013), pp.937–945.

[31] S. Malkin, Grinding technology-theory and applications of machining with abrasives, USA:Ellis Horwood Limited,1989.

[32] X. Zhou, F. Xi, Modelling and predicting surface roughness of the grinding process, International Journal of Machine Tools and Manufacture, 42(2) (2002), pp.969–977.

[33] H. K. Tonshoff, J. Peters, I. Inasaki, T. Paul, Modelling and simulation of grinding processes, Annals of the CIRP, 41(2) (1992), pp.677-688.

[34] M. J. Ren, , C. F. Cheung, L. B. Kong, X. Q. Jiang, Invariant-feature-pattern-based form characterization for the measurement of ultraprecision freeform surfaces, IEEE Transactions on Instrumentation and Measurement, 61(4) (2012), pp.963-973.

[35] Z. C. Cao, , C. F. Cheung, L. T. Ho, M.Y. Liu, Theoretical and experimental investigation of surface generation in swing precess bonnet polishing of complex three-dimensional structured surfaces, Precision Engineering, 50 (2017), pp.361-371.